Synergetic analysis of springtime air pollution episodes over Gwangju, Korea

Sung-Kyun Shin[1], Kwon-Ho Lee[1,2,*], Seung-Shik Park[3]

1)Research Institute for Radiation-Satellite (RIRS),
2)Department of Atmospheric and Environmental Sciences (DAES), Gangneung-Wonju National University(GWNU), Gangneung 25457, Republic of Korea
3)Department of Environment and Energy Engineering, Chonnam National University, Gwnagju, 61186, Republic of Korea

Submitted: October 1, 2016

Submitted to the Atmospheric Environment

* Corresponding Author;
Kwon-Ho Lee,

Department of Atmospheric and Environmental Sciences,

Ganeung-Wonju National University, Gangneung 25457, Korea

E-mail : kwonho.lee@gmail.com

Abstract

Characteristics of the springtime aerosols including vertically resolved and column integrated optical and microphysical properties were analysed during March to May of 2009 over Gwangju (35.23ºN, 126.84ºE), Korea. During the observation period, dust particles observed from a light detection and ranging (LIDAR) and CIMEL sun/sky radiometer observations showed average values of Ångström exponent at 440-870 nm wavelength pair ($Å_{440-870}$), single scattering albedo at 675 nm (Ω_{675}), depolarization ratios (δ) along with their standard deviation are 0.77 ± 0.19, 0.95 ± 0.01, and ~0.25, respectively. The elevated dust layers with high δ reached as high as 4 km above sea level. However, there is a notable feature in the characteristics of anthropogenic/smoke particles originated from the highly populated/industrialized region: relatively smaller particle size ($Å_{440-870}$ are ranged between 1.33 and 1.36) and more light-absorbing (Ω_{675} of 0.92 ± 0.01). These aerosols are mostly distributed within 1.2 km altitude. It was also found that the aerosol optical depth (AOD, τ) derived from LIDAR (τ_{LIDAR}) was in good agreement with τ from CIMEL sun/sky radiometer (τ_{CIMEL}) with a correlation coefficient of 0.7 and a bias of 15%. The comparison under the lower PM_{10} levels (<100 $\mu g/m^3$) shows less root-mean square difference (RMSD) (10%), suggests the LIDAR derived vertical aerosol extinction (α) data can accurately estimate continuous instantaneous τ under specific atmospheric conditions. These findings will further be used for quantification of the multi-dimensional air quality as well as for aviation and port services.

Key words: LIDAR, Sun/sky Radiometer, MODIS, optical/microphysical properties, Aerosol optical depth

1. Introduction

It is well known that atmospheric aerosols interfere with the solar radiation incident on Earth by scattering and absorption, thus Earth's temperature and climate can be altered by the direct aerosol radiative forcing (Bellouin et al., 2013; Griggs and Noguer, 2002). The atmospheric aerosols can also affect the Earth's climate system indirectly by acting as cloud condensation nuclei (CCN), thus the cloud and precipitation can further influence to the earth radiation budget (Penner et al., 2004; Ramanathan et al., 2001). Although research have been conducted worldwide about the potential climatic effect of the atmospheric aerosols (Huebert et al., 2003; Ramanathan and Feng, 2009), there still remain significant uncertainties with regard to the scientific understanding of their impact on climate due to the variety of shape, composition size, its spatial/temporal variation, and other properties of aerosols (Satheesh and Moorthy, 2005).

As a major source region of atmospheric aerosol, East Asia has been extensively researched in aerosol and climate interaction issues (Lee et al., 2007b; Li et al., 2007; Menon et al., 2002; Ramanathan et al., 2007), especially on some episodes, e.g. severe aerosol events of Asian dust storm from Taklamakan desert of China and the Gobi desert of Inner Mongolia (Huang et al., 2006) and smoke from boreal forest fire (Chin et al., 2002; Ginoux et al., 2004; Lee et al., 2006). Moreover, as the rapidly industrialization and popularization, e.g., the rapid development in China with economic growth, East Asia is subjected to significantly increasing concentration of aerosols from industrial and agricultural activities (Carrico et al., 2003; Huang et al., 2012). These aerosols are primarily concerned with the air quality and radiative effects determined by their microphysical and optical properties (Bates et al., 1998; Che et al., 2014; Chylek et al., 2005, 2003).useful for quantifying the characteristics of atmospheric aerosols. To date, a large number of the observations based on the integrated remote sensing techniques including a light detection and ranging (LIDAR) technique have been conducted to characterize the aerosol over East Asia (Anderson et al., 2003; Kim et al., 2014; Lee et al., 2007a; Seo et al., 2015). However, the information on the aerosol optical properties retrieved from LIDAR is still limited due to its uncertainty. Moreover, a long-term observation with LIDAR is limited with respect to the lack of a number of LIDAR station in Korea. The aerosol optical depth (AOD, τ), defined as the integral form of aerosol extinction (α) along an atmospheric column, is most widely used parameter to evaluate the distribution of atmospheric aerosol extensively. α measured from the LIDAR observation can be applied for the calculation of τ_{LIDAR}.

In this study, we used the integrated remote sensing techniques including LIDAR, sun/sky radiometer (CIMEL Electronique S.A.S, France), and satellite observation e.g. XXX at Gwangju, Korea (35.23°N, 126.84°E) (see Fig. 1) to obtain the columnar optical and microphysical properties of aerosols affecting the local atmospheric environment during spring season (March to May) of 2009. The vertical distribution of optical and microphysical properties of aerosols, and the source regions influenced on the high-PM_{10} events were investigated. For columnar characteristics of aerosols, we also estimated the τ_{LIDAR} from the vertically resolved α values and it was compared with the τ_{CIMEL} by CIMEL sun/sky radiometer. The factors that influence the variation of τ_{LIDAR} were also discussed. This paper is constructed as follow. Section 2 presents the instruments used in this study and the method to calculate the τ. Section 3 illustrates the results and findings. Discussion and conclusion can be found in Section 4.

2. Measurements

Measurements of atmospheric aerosols using a LIDAR, sun/sky radiometer, and Beta gauge were performed at Gwangju, the south-western part of the Korean peninsula (see Fig. 1) during spring season (March to May) of 2009. Gwangju is a city surrounded by mountains and is populated city (approximately 1.4 million). A residential, highway, rural, and small industrial areas are nearby the observation site. The observation site frequently experiences air pollution and Asian dust storm in spring season (Noh et al., 2008; Shin et al., 2015; Tatarov et al., 2012). The altitude of the LIDAR station is about 53 m above sea level. The aerosol parameters used in this study, and the available data are summarized in Table 1. Detailed descriptions on each instrument are following.

2.1 LIDAR retrieval of vertical information

The dual polarization LIDAR was used in this study to measure the vertical profiles of aerosol optical properties such as α, and depolarization ratio (δ). Fig. 2 shows a sketch of the LIDAR in its configuration. This LIDAR uses a pulsed Nd:YAG laser as a light source at the wavelength of 1064 nm. A retarder allows for generating linear-polarized laser light at 532 nm wavelength. The laser beam (170 mJ at 532 nm, a repetition rate of 10 Hz) is transmitted vertically into the atmosphere after expanding five-fold by the beam expander. The backscattered signals are then collected by an 8-inch Schmidt-Cassegrain type telescope with 60 MHz sampling rate. These signals are transmitted through an interference filter and a polarizing beam splitter (PBS) separates the co-polarized signals from the cross-polarized signal. The polarized signals enter into the photomultiplier tube (PMT) generating electronic signals and consequently saved as the digital data. These data are collected within 2 minutes having a 2.5 m vertical resolution, and the lowest height of complete overlap height of LIDAR is 250 m. More detailed description of this LIDAR instrument was also given by Shin et al. (2014).

Total signal for a typical elastic scattering LIDAR is described by the LIDAR general equation as:

$$\mathrm{P(Z)} = \mathrm{P_0}\frac{\mathrm{ct}}{2}\mathrm{A}\frac{\beta(\mathrm{z})}{\mathrm{z}^2}\exp[-2\int_0^{\mathrm{z}}\alpha\,(\mathrm{z}')\mathrm{dz}']. \qquad (1)$$

where P(z) is the received signal from a distance z. P_0 is the power of laser, c is the speed of light, t is pulse duration, A is the system calibration factor including the area of the telescope's outer lens that is responsible for the collection of backscattered light and efficiency of detector. $\beta(z)$ is the backscatter coefficient determined by the strength of the LIDAR signal and it describes how much light is scattered into the backward direction. α is the extinction coefficient occurred by scattering and absorption of light by molecules and particles (Wandinger, 2005). Equation (1) can be solved on a basis of the numerical inversion scheme suggested by Klett (1985, 1981). In this scheme, assumptions of the extinction to backscatter ratio (so-called lidar ratio, *S*) and the reference value of the β at a certain height are required to derive α. In general, the reference height of the backscatter profile of the raw signals is set in an altitude where the atmosphere is assumed as aerosol free regions. To overcome the uncertainty owing to unknown *S*, we used the information on so-called aerosol types with the δ. The δ is useful parameter for the identification of particle shape. For instance, non-spherical particle such as dust, sea-salt, and ice cloud has high δ. Anthropogenic aerosols are normally spherical with small δ (Murayama et al., 2004; Shin et al., 2015). In this study, we used the *S* from 45 sr to 90 sr at 532 nm (Burton et al., 2012; Müller et al., 2007) according to the aerosol type which is classified with the δ.

The LIDAR can measure the parallel polarized and perpendicular polarized signals at 532 nm which are used for derivation of the total depolarization ratio (δ_{tot}). In this contribution, aerosol depolarization ratio (δ) was derived from the δ_{tot} and the backscatter ratio (R) in order to remove signal contributed by air molecules (Shin et al., 2014).

$$\delta = \frac{\delta_{tot}R - \delta_{mol}}{R-1}. \tag{2}$$

where R is defined as (β_a+ β_a)/ β_m. β_a and β_m denote the β of atmospheric aerosols and atmospheric molecules, respectively. δ_{mol} is the molecular depolarization ratio. We use a constant δ_{mol} of 0.014 (Cairo et al., 1999).

After determination of α profiles, we derived τ_{LIDAR} by integrating α with height. The τ can be simply expressed as:

$$\tau_{\mathrm{LIDAR}} = \int_{z_1}^{z_2} \alpha_a(z)dz. \quad (3)$$

where, z_1 and z_2 is the bottom height and top height of an atmospheric vertical column, respectively.

The scaling height ($Z_{S.H}$) is also retrieved in order to investigate the vertical distribution of aerosol layer. $Z_{S.H}$ presents that the vertical points of an exponential aerosol profile at which aerosols starts to be decreased exponentially as:

$$\alpha_a(z) = \alpha_a(z = 0)\exp(-\frac{z}{z_{S.H}}) \quad (4)$$

where, $\alpha_a(z)$ is the extinction coefficient at a given altitude z km. By using equation (3) with equation (4), $Z_{S.H}$ can be derived. The smaller $Z_{S.H}$ indicates that the aerosols are distributed around the lower troposphere or the surface, whereas the larger $Z_{S.H}$ is considered that the aerosols are mainly contributed in upper troposphere for the condition that the amount of aerosols is same (Qiu et al., 2005; Wong et al., 2009). $Z_{S.H}$ could be determined by columnar τ and α at the surface (Lee et al., 2014; Shin and Lee, 2016).

2.2 CIMEL sun/sky radiometer measurement

In order to validate and compare τ_{LIDAR}, we used τ_{CIMEL} from the polarized-version of the CIMEL 381-1 automatic sun-tracking sun/sky radiometer. This sun/sky radiometer measures the radiances in five spectral channels (440, 500, 675, 870, and 1020 nm). Direct solar radiation at 15-miniutes intervals and sky radiation at 1-hour interval are obtained. The data obtained by the sun/sky radiometer are sent to NASA Goddard Space Centre for retrieval of aerosol optical/microphysical properties with AERONET algorithm (Holben et al., 1998). The data are available to at the webpage of AERONET database (http://aeronet.gsfc.nasa.gov/). The quality of data is assured thorough the regular validation and calibration (Holben et al., 2006). In this study, we used the level 2.0 quality assured τ_{CIMEL} data. Because of the CIMEL 381-1 sun/sky radiometer does not provide the τ at 532 nm, we obtained the τ_{CIMEL} at 532 nm via a relation between τ_{CIMEL} and Ångström exponent (Å) as flow:

$$\tau_{\mathrm{CIMEL,532}} = \tau_{\mathrm{CIMEL,500}}\left(\frac{\lambda_{532}}{\lambda_{500}}\right)^{-\text{Å}_{440-870}} \tag{5}$$

where, we used the values of the Å retrieved from 440 nm/870 nm wavelength pair ($\text{Å}_{440\text{-}870}$) in this study.

The microphysical properties such as single scattering albedo (Ω), asymmetric factor (*g*), refractive indices are also obtained from AERONET. Detailed information on the data retrieval algorithm is given in Dubovik and King (2000). These microphysical properties of aerosol are also used to investigate the characteristics of atmospheric aerosol observed during observation periods.

2.3 PM_{10} measurement

Hourly-averaged PM_{10} concentrations, measured routinely at the Gwangju

Meteorological Administration (GMA), were used to investigate the temporal variation of PM_{10} concentration during this measurement period. The PM_{10} concentrations are measured by beta (β)-ray absorption method with a PM_{10} beta gauge (PM_{10} B.G., W&A Inc., U.S.). The GMA is located within a maximum distance of approximately 5.5 km from the LIDAR and AERONET sun/sky radiometer observation site.

In order to investigate the relationship between vertically integrated τ and the surface PM_{10} concentrations, each measurement was collocated both spatially and temporally. Such comparison is only valid for daytime because AERONET sun/sky radiometer measurements are only carried out during daytime. Also, each data measured within 15 minutes were selected for the comparison.

2.4 Satellite observation

Terra and Aqua MODIS level 1B (L1B) calibrated radiance dataset, namely MOD02 and MYD02 products (collection 6), were acquired from the NASA Goddard Earth Science Distributed Active Archive Center (DAAC). MODIS L1B dataset contains calibrated and geolocated at-aperture radiances in W/m^2/μm/sr for 36 bands across a 2,330 km wide swath. Temporal coverage for the daily data spans the following periods: Mar to May 2009. To derive τ_{MODIS} from the MODIS L1B data, the MODIS satellite aerosol retrieval (MSTAR) algorithm (Lee et al., 2006; 2007a; Lee and Kim, 2010) is used. MSATR has been developed for the acquisition of fine resolution τ_{MODIS} based on look-up table approach. By using a general radiative transfer equation, τ_{MODIS} is determined by comparing the MODIS observed aerosol reflectances (ρ_{Aer}) with pre-calculated values.

$$\rho_{Aer}(\theta_0,\theta_S,\varphi)=\rho_{TOA}(\theta_0,\theta_S,\varphi)-\rho_{Ray}(\theta_0,\theta_S,\varphi)-\frac{T_{Tot}(\theta_0)\cdot T_{Tot}(\theta_S)\cdot\rho_{Surf}(\theta_0,\theta_S)}{1-\rho_{Surf}(\theta_0,\theta_S)\cdot r_{Hem}(\tau_{Tot},g)} \tag{6}$$

where ρ_{Ray} and ρ_{Surf} are the reflectances by the Rayleigh scattering and surface. θ_0, θ_S, φ are sun zenith angle, satellite viewing angle, relative azimuth angle between sun and satellite. τ_{Tot} represent total optical thickness of atmosphere, T_{Tot} the total atmospheric transmittance, g the asymmetry parameter, and r_{Hem} the hemispheric reflectance, respectively. The retrieval error of the τ_{MODIS} by the MSTAR algorithm was reported to be <10% (Lee and Kim, 2010).

3. Results

Fig. 3 shows the temporal variation of PM_{10} concentration, $Å_{440-870}$, and precipitable water contents (PWC) which are obtained from AERONET. During the observation period, the high-PM_{10} episodes were measured. PM_{10} concentration was peaked as high as 139 $\mu g/m^3$, 134 $\mu g/m^3$, and 89 $\mu g/m^3$ on 16 March 2009, 8 April 2009, and 6 May 2009, respectively. Based on these information, we classified the observation periods into three cases according to these high-PM_{10} episodes (e.g., Episode I : 15~16 March 2009, Episode II : 5~12 April 2009, Episode III : 5~7 May 2009). The maximum PM_{10} concentrations in these three episodes were recorded. It is considered that the aerosols significantly affect to the atmospheric environment at the observation site.

Besides, the values of $Å_{440-870}$ measured during each individual high-PM_{10} episode were remarkably differed. For instance, high values of Å (>1) typically represent the accumulation mode particles such as fresh biomass-burning particles. In contrast, low Å values close to 0 are observed for coarse mode particles such as Asian dust (Chen et al., 2009; Franke et al., 2003; Sakai et al., 2002). The lower values of $Å_{440-870}$ which are measured during Episode I are considered as it contains more coarse-mode particles such as dust. In contrast, the higher values of $Å_{440-870}$ for Episode II and III might be considered to contain the fine-mode particles dominantly.

In consideration of the hygroscopic growth of particle, aerosol size can change with relative humidity of the atmospheric environment with an assumption that the composition of atmospheric aerosol is nearly constant. Mean values of PWC measured are 0.53 ± 0.32 cm, 0.77 ± 0.32 cm, 0.81 cm, and 1.04 ± 0.45 cm for the episode I, II, III and the others, respectively. The corresponding values are summarized in Table 2. These PWC values are significantly lower than the mean values of PWC measured even in dry season over East Asia. Mean PWC during a spring season in China is reported as 1.93 cm and 2.2 to 2.6 cm in the dry season in northern Indochina (Zhai and Eskridege, 1997). Therefore, the aerosols observed in this study are less influenced by the moisture (i.e., less hygroscopic growth) during this season.

For the estimation of the spatial pattern of aerosols, satellite derived aerosol data has been compared. Fig. 4 shows MODIS-retrieved τ at 550 nm combined MODIS RGB (red, blue, green) colour composite image of North-East Asia for each individual episode.

In episode I, a thick Asian dust plume over East China is clearly seen in Fig. 4a-4c. High τ values ranging from 0.8 to 2.4 over this region indicate that strong Asian dust plumes were transported from China to the Korean peninsula. These events are considered as results from the transportation of this Asian dust case. On the other hands, high τ were observed over industrialized/populated regions of China for the episode II (Fig. 4d-4f). These high τ from China might lead the high-PM_{10} events occurred in the episode II. However, high-PM_{10} occurred during the episode III seems not to be affected by the transportation of atmospheric aerosol from China (Fig. 4g-4i).

The Hybrid Single Particle Lagrangian Integrated Trajectory (HYSPLIT) model (Draxler and Hess, 1998) with archived National Centers for Environmental Prediction-National Center for Atmospheric Research (NCEP-NCAR) reanalysis data is used to investigate the backward trajectories of air masses that reached the observation site. We used 120-hour backward trajectory conditions for the arrival height of each aerosol layer during each high-PM_{10} episode. The results of the HYSPLIT model calculation are shown in Fig. 5. There are clear differences between transport routes of air masses according to the HYSPLIT results. As shown in Fig. 5a, HYSPLIT model calculation results show that the air mass mainly originates from desert area in Asian continent for the episode I. Nevertheless, the air masses that observed during the episode II had predominantly passed over industrial regions of China before arrival at the observation (Fig. 5b). Moreover, vertical positions of air masse during the episode II are significantly distinguished from the trajectories during the episode I. From these results, the air masses were transported through the near lower troposphere (<2 km) over Chinese industrialized areas in the episode II, whereas the air masses during the episode II were passed over these region at high altitude levels (>2 km). Former study also reported that anthropogenic aerosols are transported when air masses were passed near the surface or within the lower troposphere over industrialized areas (Shin et al., 2015). On the other hand, the trajectory lines during the episode III have followed a path over the Korean peninsula with a longer transportation time as shown in Fig. 5c. High PM_{10} concentrations in the episode III are more likely to be originated from local emission source of Korea.

Fig. 6 shows the time-height distribution of the range-corrected backscatter signal and the δ acquired during the entire observation period. In case of rain events, measurements were automatically interrupted. A precipitation sensor assures a proper shut down of the LIDAR observation during rain event.

Intensity of δ can be used for the identification of aerosol type. For example, high δ (~0.3) indicates nearly pure dust (Freudenthaler et al., 2009; Sugimoto and Lee, 2006) while lower δ represents the increase of spherical particles such as urban aerosols (Burton et al., 2013). From the Lidar observations, the aerosol layers have high δ of more than 0.4, which is observed frequently above 5 km is during observation period, are considered as ice cloud (Sakai et al., 2003). Likewise, the aerosol layer observed around 2 km for the episode I includes dust particles dominantly with high δ (~0.25). In contrast, lower δ (<0.10) measured in both episode II and III below 1.5 km altitude is similar to the values of δ for anthropogenic aerosols or biomass burning aerosols which are reported in previous studies (Burton et al., 2013; Chen et al., 2009).

In Fig. 6, the vertical distributions of range-corrected signal showed that the most aerosol layers were distributed within 1~2 km during the observation period. However, significantly different aerosol layers are found for each episode. Fig. 7 shows the mean vertical profiles of α measured from the LIDAR for the classified episodes, respectively. The observed aerosol layers are mostly distributed around 1.2 km. In contrast the aerosol layers which are considered as dust-dominant, inferred with higher δ (Episode I), were existed between 1.5 km and 4.0 km. This result represents that the dust particles are frequently transported and distributed above planetary boundary layer (PBL), for example above 2 km during the observation system. However, the anthropogenic aerosols are distributed mainly within the PBL either near surface.

The vertical distributions estimated from $Z_{S.H}$ are in comparably good agreement with the vertical distribution of aerosols retrieved from LIDAR for each episode. The average value of the $Z_{S.H}$ is 2.06 ± 0.36 km, 1.23 ± 0.42 km, 1.45 ± 0.46 km, and 1.29 ± 0.62 km altitude for the episode I, episode II, the episode III, and the others, respectively.

In order to investigate the microphysical properties such as Ω, *g*, and the refractive index of aerosols measured during observation period, the level 2.0 inversion products of AERONET are used. Fig. 8 shows the Ω, the g, and the real part (*n*) and the imaginary part (*k*) of the refractive index at 440, 675, 870, and 1020 nm obtained from AERONET for each classified episode during the observation period. The corresponding values are summarized in Table 3.

The aerosols with Ω higher than 0.95 are considered as lower light-absorbing aerosol, whereas, the aerosols with Ω lower than 0.88 are considered higher light-absorbing aerosol

(Abel et al., 2003). Ω of aerosol for each classified episode in this study is significantly differed. The higher Ω for the episode I was higher than other cases. The mean value of Ω for the episode I was 0.92 ± 0.01, 0.95 ± 0.01, 0.96 ± 0.01, and 0.96 ± 0.01 at 440, 675, 870, and 1020 nm, respectively. Ω for the episode I are similar to the values of Ω for pure dust (0.96 at 500 nm, 0.94~0.98 at 440, 675, 870, and 1020 nm) reported in previous studies (Mikami et al., 2006; Yu et al., 2006). In contrast with this, the mean values of Ω for the episode II and the episode III were 0.93 ± 0.01, 0.92 ± 0.01, 0.91 ± 0.01, and 0.89 ± 0.02 and 0.92 ± 0.01, 0.92 ± 0.01, 0.92 ± 0.01, and 0.92 ± 0.01 at 440, 675, 870, and 1020 nm, respectively. Eck et al. (2009) reported that black carbon particle have the strongest absorption in the near-infrared region in the spectrum, whereas aerosols composed of brown carbon or organic carbon which has strong light-absorption properties in the ultraviolet and visible regions. We believe that the aerosol layers observed during the episode II are more likely to contain the more black carbon particles. Black carbon might be transported from the industrialized region of China to the observation site. The aerosol layers for the episode III are considered as it includes more brown carbon or organic carbon, which is originated from domestic source regions, than other cases.

g is the fraction of the incident light scattered forward after striking a particle. When 100% of the incident light is scattered forward, *g* is close to 1. *g* is 0 if one half of the incident light is forward-scattered and the other half is backscattered. *g* is decreased as the wavelengths increase for the spherical-like particle such as biomass burning aerosol reported by Dubovik et al. (2002). *g* seems not to be decreased as the wavelength increases for both the episode I. However, remarkable reduction in the spectrum of *g* with increment of wavelength was found for both episode II and III. That means both episodes are more likely to be affected by the aerosols from biomass burning.

Real part of the refractive index (*n*) measured during the entire observation periods are higher than the values of *n* for biomass burning/smoke aerosol particles reported in the range between 1.41 and 1.44 (Noh et al., 2011). On the other hand, the averaged value of n for the episode I, which is considered as dust-dominant, is measured as slightly lower than n for the desert dust (1.48 ± 0.05~1.56 ± 0.03) reported in previous studies (Dubovik et al., 2002; Noh et al., 2011). The mean value of the imaginary part of the refractive index (k) for the episode I is remarkably lower than the other episodes. The averaged values of the k for the episode I are 0.0046 ± 0.0002, 0.0026 ± 0.0003, 0.0025 ± 0.0003, and 0.0027 ± 0.0001 at 440, 675, 870, and 1020 nm, respectively. The k for the episode I is similar to the values of the k for the desert dust reported as 0.0025~0.0029, 0.0013~0.0014, 0.001, and 0.001 at 440, 670, 870, and 1020 nm (Dubovik et al., 2002). It is considered that characteristics of Asian dust particle, which is more likely to scatter, reflect the values of k for the episode I. In contrast with this, the value of k for the episode II was highest. It is considered that the aerosol layers observed during this episode contains more light-absorbing particles such as smoke particles and anthropogenic particles.

Fig. 9 shows the temporal variation of the τ_{LIDAR} and τ_{CIMEL}. τ provided from the MODIS (τ_{TERRA} for Terra and τ_{AQUA} for Aqua platforms, respectively) are also shown for comparison. Daily averaged values of τ_{TERRA} and τ_{AQUA}, which were obtained and averaged within a 55 km diameter centred over the CIMEL sun/sky radiometer and LIDAR observation site, are used. The corresponding values are given in Table 4. τ_{LIDAR} are calculated from the vertical profiles of α using equation (3). Ranges of integration were set from the surface to the height that the aerosols exist. α below overlap height > 250 m were assumed that aerosols are well mixed below 250 m, thus the values of α are from 250 m to the surface are constant. We excluded the observation date when the cirrus cloud or water droplet cloud is observed for the τ retrieval.

The average value of τ_{LIDAR} at 532 nm for the episode I is 0.52 ± 0.20. Mean value of τ_{CIMEL} at 532 nm inferred from τ at 500 nm data with the $Å_{440\text{-}870}$ data from the AERONET is 0.71 ± 0.42. Mean τ_{TERRA} is 0.77 ± 0.11 for Episode I. With regard to the episode II, mean values of τ_{LIDAR}, τ_{CIMEL}, τ_{TERRA}, and τ_{AQUA} are 0.44 ± 0.14, 0.68 ± 0.26, 0.66 ± 0.14, and 0.70 ± 0.16, respectively. τ_{LIDAR}, τ_{CIMEL}, τ_{TERRA}, and τ_{AQUA} for the episode III are 0.41 ± 0.07, 0.44 ± 0.16, 0.58 ± 0.07, and 0.56 ± 0.07, respectively. These values are significantly higher than the annual mean value of τ measured by MODIS satellite over North-East Asia (0.33; Kim et al., 2013). It is considered that atmospheric environment in the spring of Korea is significantly influenced by aerosols than other season. Dust particles are particularly contributed to the increment of τ over Korea in the spring time.

Overall values of τ_{LIDAR} were measured as lower than the values of τ_{CIMEL}, τ_{TERRA}, and τ_{AQUA} during the observation period. In order to investigate the influence factor of these discrepancies between τ_{LIDAR} and τ retrieved from the other measurements, τ_{CIMEL} were used as a “ground truth” for the comparison with τ_{LIDAR} in this study. τ_{LIDAR} and τ_{CIMEL} are comparably in good agreement in a certain atmospheric condition. We found that the differences between τ_{LIDAR} and τ_{CIMEL} have a significant trend with respect to the variation of PM_{10} concentration at the surface. In Fig. 10, we presented correlation of τ_{LIDAR} with τ_{CIMEL} with regard to PM_{10} concentration. The differences between τ_{LIDAR} and τ_{CIMEL} are increased as larger PM_{10} concentrations (Fig. 10a). Root-mean square difference (RMSD) in τ was 28% when higher PM_{10} concentrations (>100 $\mu g/m^3$) are measured. On the other hands, the agreement between τ_{LIDAR} and τ_{CIMEL} goes well as PM_{10} concentration decreased (Fig. 10b). The RMSD in τ was 10% for these cases (<100 $\mu g/m^3$). The corresponding values are summarized in Table 5.

One possible reason for these differences may be the different setting for the range of atmospheric vertical column. The CIMEL sun/sky radiometer measured τ in the total atmospheric vertical column (from the surface to the top of atmosphere). In contrast, τ_{LIDAR} is calculated from the integral of the vertical profile of α. τ_{LIDAR} may have large uncertainty when the integral range is not accurately considered. Another reason may be considered as the uncertainty of α below overlap height (~250 m in this study). In this study, we assumed that α

from 250 m height to the surface are constant. τ_{LIDAR} can be retrieved reliably with this assumption if the aerosols are mixed well in this range. However, the accuracy in calculation of τ_{LIDAR} may be varied according to the distribution of aerosols. α below overlap height could be underestimated with this assumption when the aerosols are mostly distributed at the surface.

4. Summary and Conclusion

Vertical profiles of aerosol optical properties and microphysical properties were measured from the LIDAR and sun/sky radiometer at Gwangju, Korea during a spring season in 2009. The entire observation period has been divided into three air pollution episodes characterized by the relatively high-PM_{10} concentrations. δ obtained from LIDAR observations were also used to classify the type of aerosol for each categorized episode. It was found that the Asian dust layers observed in spring season of 2009 are mostly distributed around 1.5 ~ 4 km. These elevated height ranges are comparably higher than the typical anthropogenic/urban aerosols which are mostly distributed within 1.2 km. The optical characteristics of aerosols such as the Ω, the g, and the refractive indices obtained from AERONET database were also varied with respect to the type of aerosols which were transported from different sources.

After classified into three major air pollution episodes, we found distinguishable characteristics for each category. For the episode I, Asian dust was dominated with the higher values in Ω and lower values of the k. The mean values of Ω and k for this case were 0.95 ± 0.01 and 0.0026 ± 0.0003 at 675 nm, respectively. In contrast, the atmospheric aerosol observed in the episode II and III is more likely to be anthropogenic/biomass burning aerosols with lower Ω, higher reduction of g according to the increment of wavelength, lower values of n, and higher values for k. Moreover, the episode II showed the strongest light-absorbing particles such as black carbon originated from industrial/populated region.

In comparison of τ_{LIDAR} and τ_{CIMEL}, τ_{LIDAR} were in good agreement with τ_{CIMEL} in most observation cases. However, we found disagreement for a few measurements. This discrepancy could be considered as results of inaccuracy or missing of α below overlap height. Difference between the τ_{LIDAR} and τ_{CIMEL} increases when the aerosol loadings are high near surface below PBL. Our results suggest that τ_{LIDAR} should be determined carefully with the consideration of aerosol distribution near surface. In order to retrieve the accurate values of τ_{LIDAR}, we will develop the effective and reliable method for the correction of these influences. With regardless to this, the integrated remote sensing techniques by using LIDAR, sun/sky radiometer, and satellite observation is very useful for the characterization of atmospheric aerosols. Moreover, the aerosol parameters obtained from each individual instrument could be used for not only the comparison or the validations but also the inter-compensation of the limitation of each instrument.

Acknowledgements

This work was funded by the Korea Meteorological Administration Research and Development Program under Grant KMIPA2015-2012.

References

Abel, S.J., Haywood, J.M., Highwood, E.J., Li, J., Buseck, P.R., 2003. Evolution of biomass burning aerosol properties from an agricultural fire in southern Africa. Geophysical Research Letters 30. doi: 10.1029/2003GL017342.

Anderson, T.L., Masonis, S.J., Covert, D.S., Ahlquist, N.C., Howell, S.G., Clarke, A.D., McNaughton, C.S., 2003. Variability of aerosol optical properties derived from in situ aircraft measurements during ACE-Asia. Journal of Geophysical Research: Atmospheres 108. doi: 10.1029/2002JD003247.

Bates, T.S., Huebert, B.J., Gras, J.L., Griffiths, F.B., Durkee, P.A., 1998. International Global Atmospheric Chemistry (IGAC) project's first aerosol characterization experiment (ACE 1): Overview. Journal of Geophysical Research: Atmospheres 103, 16297-16318. doi: 10.1029/97JD03741.

Bellouin, N., Quaas, J., Morcrette, J.-J., Boucher, O., 2013. Estimates of aerosol radiative forcing from the MACC re-analysis. Atmospheric Chemistry and Physics 13, 2045-2062. doi: 10.5194/acp-13-2045-2013.

Burton, S., Ferrare, R., Hostetler, C., Hair, J., Rogers, R., Obland, M., Butler, C., Cook, A., Harper, D., Froyd, K., 2012. Aerosol classification using airborne High Spectral Resolution Lidar measurements–methodology and examples. Atmospheric Measurement Techniques 5, 73-98. doi: 10.5194/amt-5-73-2012.

Burton, S., Ferrare, R., Vaughan, M., Omar, A., Rogers, R., Hostetler, C., Hair, J., 2013.

Aerosol classification from airborne HSRL and comparisons with the CALIPSO vertical feature mask. Atmospheric Measurement Techniques 6, 1397-1412. doi: 10.5194/amt-6-1397-2013.

Cairo, F., Di Donfrancesco, G., Adriani, A., Pulvirenti, L., Fierli, F., 1999. Comparison of various linear depolarization parameters measured by lidar. Applied Optics 38, 4425-4432. doi: 10.1364/AO.38.004425.

Carrico, C.M., Kus, P., Rood, M.J., Quinn, P.K., Bates, T.S., 2003. Mixtures of pollution, dust, sea salt, and volcanic aerosol during ACE-Asia: Radiative properties as a function of relative humidity. Journal of Geophysical Research: Atmospheres 108. doi: 10.1029/2003JD003405.

Che, H., Xia, X., Zhu, J., Li, Z., Dubovik, O., Holben, B., Goloub, P., Chen, H., Estelles, V., Cuevas-Agulló, E., 2014. Column aerosol optical properties and aerosol radiative forcing during a serious haze-fog month over North China Plain in 2013 based on ground-based sunphotometer measurements. Atmospheric Chemistry and Physics 14, 2125-2138. doi: 10.5194/acp-14-2125-2014.

Chen, W.-N., Chen, Y.-W., Chou, C.C., Chang, S.-Y., Lin, P.-H., Chen, J.-P., 2009. Columnar optical properties of tropospheric aerosol by combined lidar and sunphotometer measurements at Taipei, Taiwan. Atmospheric Environment 43, 2700-2708. doi: 10.1016/j.atmosenv.2009.02.059.

Chin, M., Ginoux, P., Kinne, S., Torres, O., Holben, B.N., Duncan, B.N., Martin, R.V., Logan, J.A., Higurashi, A., Nakajima, T., 2002. Tropospheric aerosol optical thickness from the GOCART model and comparisons with satellite and Sun photometer measurements. Journal of the atmospheric sciences 59, 461-483. doi: 10.1175/1520-0469(2002)059<0461:TAOTFT>2.0.CO;2.

Chylek, P., Henderson, B., Mishchenko, M., 2003. Aerosol radiative forcing and the accuracy of satellite aerosol optical depth retrieval. Journal of Geophysical Research: Atmospheres 108. doi: 10.1029/2003JD004044.

Chylek, P., Henderson, B.G., Lesins, G., 2005. Aerosol optical depth retrieval over the NASA Stennis Space Center: MTI, MODIS, and AERONET. Geoscience and Remote Sensing, IEEE Transactions on 43, 1978-1983. doi: 10.1109/TGRS.2005.851773.

Draxler, R.R., Hess, G., 1998. An overview of the HYSPLIT_4 modelling system for trajectories. Australian meteorological magazine 47, 295-308.

Dubovik, O., Holben, B., Eck, T.F., Smirnov, A., Kaufman, Y.J., King, M.D., Tanré, D., Slutsker, I., 2002. Variability of absorption and optical properties of key aerosol types observed in worldwide locations. Journal of the atmospheric sciences 59, 590-608. doi: 10.1175/1520-0469(2002)059<0590:VOAAOP>2.0.CO;2.

Dubovik, O., King, M.D., 2000. A flexible inversion algorithm for retrieval of aerosol optical properties from Sun and sky radiance measurements. Journal of Geophysical Research 105, 20673-20696. doi: 10.1029/2000JD900282.

Eck, T., Holben, B., Reid, J., Sinyuk, A., Hyer, E., O'Neill, N., Shaw, G., Vande Castle, J., Chapin, F., Dubovik, O., 2009. Optical properties of boreal region biomass burning aerosols in central Alaska and seasonal variation of aerosol optical depth at an Arctic coastal site. Journal of Geophysical Research: Atmospheres 114. doi: 10.1029/2008JD010870.

Franke, K., Ansmann, A., Müller, D., Althausen, D., Venkataraman, C., Reddy, M.S., Wagner, F., Scheele, R., 2003. Optical properties of the Indo-Asian haze layer over the tropical Indian Ocean. Journal of Geophysical Research: Atmospheres 108. doi: 10.1029/2002JD002473.

Freudenthaler, V., Esselborn, M., Wiegner, M., Heese, B., Tesche, M., Ansmann, A., Müller, D., Althausen, D., Wirth, M., Fix, A., 2009. Depolarization ratio profiling at several wavelengths in pure Saharan dust during SAMUM 2006. Tellus B 61, 165-179. doi: 10.1111/j.1600-0889.2008.00396.x.

Ginoux, P., Prospero, J.M., Torres, O., Chin, M., 2004. Long-term simulation of global dust distribution with the GOCART model: correlation with North Atlantic Oscillation. Environmental Modelling & Software 19, 113-128. doi: 10.1016/S1364-8152(03)00114-2.

Griggs, D.J., Noguer, M., 2002. Climate change 2001: the scientific basis. Contribution of working group I to the third assessment report of the intergovernmental panel on climate change. Weather 57, 267-269. doi: 10.1256/004316502320517344.

Holben, B., Eck, T., Slutsker, I., Smirnov, A., Sinyuk, A., Schafer, J., Giles, D., Dubovik, O., 2006. AERONET's version 2.0 quality assurance criteria, Asia-Pacific Remote Sensing Symposium. International Society for Optics and Photonics, pp. 64080Q-64080Q-64014. doi: 10.1117/12.706524.

Holben, B., Eck, T., Slutsker, I., Tanre, D., Buis, J., Setzer, A., Vermote, E., Reagan, J., Kaufman, Y., Nakajima, T., 1998. AERONET—A federated instrument network and data archive for aerosol characterization. Remote sensing of environment 66, 1-16. doi: 10.1016/S0034-4257(98)00031-5.

Huang, J., Minnis, P., Lin, B., Wang, T., Yi, Y., Hu, Y., Sun-Mack, S., Ayers, K., 2006. Possible influences of Asian dust aerosols on cloud properties and radiative forcing observed from MODIS and CERES. Geophysical Research Letters 33. doi: 10.1029/2005GL024724.

Huang, X., Song, Y., Li, M., Li, J., Zhu, T., 2012. Harvest season, high polluted season in East China. Environmental Research Letters 7, 044033. doi: 10.1088/1748-9326/7/4/044033.

Huebert, B.J., Bates, T., Russell, P.B., Shi, G., Kim, Y.J., Kawamura, K., Carmichael, G., Nakajima, T., 2003. An overview of ACE-Asia: Strategies for quantifying the relationships between Asian aerosols and their climatic impacts. Journal of Geophysical Research: Atmospheres 108. doi: 10.1029/2003JD003550.

Kim, H.-S., Chung, Y.-S., Lee, S.-G., 2013. Analysis of spatial and seasonal distributions of MODIS aerosol optical properties and ground-based measurements of mass concentrations in the Yellow Sea region in 2009. Environmental monitoring and assessment 185, 369-382. doi: 10.1007/s10661-012-2559-3.

Kim, J., Yum, S., Shim, S., Kim, W., Park, M., Kim, J.-H., Kim, M.-H., Yoon, S.-C., 2014. On the submicron aerosol distributions and CCN number concentrations in and around the Korean Peninsula. Atmospheric Chemistry and Physics 14, 8763-8779. doi: 10.5194/acp-14-8763-2014.

Klett, J.D., 1981. Stable analytical inversion solution for processing lidar returns. Applied Optics 20, 211-220. doi: 10.1364/AO.20.000211.

Klett, J.D., 1985. Lidar inversion with variable backscatter/extinction ratios. Applied Optics 24, 1638-1643. doi: 10.1364/AO.24.001638.

Lee, K.H., Kim, Y.J., Kim, M.J., 2006. Characteristics of aerosol observed during two severe haze events over Korea in June and October 2004. Atmospheric Environment 40, 5146-5155. doi: 10.1016/j.atmosenv.2006.03.050.

Lee, K.H., Kim, Y.J., von Hoyningen-Huene, W., Burrow, J.P., 2007a. Spatio-temporal variability of satellite-derived aerosol optical thickness over Northeast Asia in 2004. Atmospheric Environment 41, 3959-3973. doi: 10.1016/j.atmosenv.2006.03.050.

Lee, K.H., Li, Z., Wong, M.S., Xin, J., Wang, Y., Hao, W.M., Zhao, F., 2007b. Aerosol single scattering albedo estimated across China from a combination of ground and satellite measurements. Journal of Geophysical Research: Atmospheres 112. doi: 10.1029/2007JD009077.

Lee, K.H., Kim, Y.J., 2010. Satellite remote sensing of Asian aerosols: a case study of clean, polluted and dust storm days, Atmos. Meas. Tech. 3, 1771-1784, doi:10.5194/amt-3-1771-2010.

Lee, K.H., Wong, M.S., Kim, K., Park, S.S., 2014. Analytical approach to estimating aerosol extinction and visibility from satellite observations. Atmospheric Environment 91, 127-136. doi: 10.1016/j.atmosenv.2014.03.050.

Li, Z., Niu, F., Lee, K.H., Xin, J., Hao, W.M., Nordgren, B., Wang, Y., Wang, P., 2007. Validation and understanding of Moderate Resolution Imaging Spectroradiometer aerosol products (C5) using ground-based measurements from the handheld Sun photometer network in China. Journal of Geophysical Research: Atmospheres 112. doi: 10.1029/2007JD008479.

Menon, S., Hansen, J., Nazarenko, L., Luo, Y., 2002. Climate effects of black carbon aerosols in China and India. Science 297, 2250-2253. doi: 10.1126/science.1075159.

Mikami, M., Shi, G., Uno, I., Yabuki, S., Iwasaka, Y., Yasui, M., Aoki, T., Tanaka, T., Kurosaki, Y., Masuda, K., 2006. Aeolian dust experiment on climate impact: An overview of Japan–China joint project ADEC. Global and Planetary Change 52, 142-172. doi: 10.1016/j.gloplacha.2006.03.001.

Müller, D., Ansmann, A., Mattis, I., Tesche, M., Wandinger, U., Althausen, D., Pisani, G., 2007. Aerosol-type-dependent lidar ratios observed with Raman lidar. Journal of Geophysical Research: Atmospheres 112. doi: 10.1029/2006JD008292.

Murayama, T., Müller, D., Wada, K., Shimizu, A., Sekiguchi, M., Tsukamoto, T., 2004. Characterization of Asian dust and Siberian smoke with multi-wavelength Raman lidar over Tokyo, Japan in spring 2003. Geophysical Research Letters 31. doi: 10.1029/2004GL021105.

Noh, Y.M., Kim, Y.J., Müller, D., 2008. Seasonal characteristics of lidar ratios measured with a Raman lidar at Gwangju, Korea in spring and autumn. Atmospheric Environment 42, 2208-2224. doi: 10.1016/j.atmosenv.2007.11.045.

Noh, Y.M., Müller, D., Mattis, I., Lee, H., Kim, Y.J., 2011. Vertically resolved light-absorption characteristics and the influence of relative humidity on particle properties: Multiwavelength Raman lidar observations of East Asian aerosol types over Korea. Journal of Geophysical Research: Atmospheres 116. doi: 10.1029/2010JD014873.

Penner, J.E., Dong, X., Chen, Y., 2004. Observational evidence of a change in radiative forcing due to the indirect aerosol effect. Nature 427, 231-234. doi: 10.1038/nature02234.

Qiu, J., Zong, X., Zhang, X., 2005. A study of the scaling height of the tropospheric aerosol and its extinction coefficient profile. Journal of Aerosol Science 36, 361-371. doi: 10.1016/j.jaerosci.2004.10.005.

Ramanathan, V., Crutzen, P., Kiehl, J., Rosenfeld, D., 2001. Aerosols, climate, and the hydrological cycle. Science 294, 2119-2124. doi: 10.1126/science.1064034.

Ramanathan, V., Feng, Y., 2009. Air pollution, greenhouse gases and climate change: Global and regional perspectives. Atmospheric Environment 43, 37-50. doi: 10.1016/j.atmosenv.2008.09.063.

Ramanathan, V., Li, F., Ramana, M., Praveen, P., Kim, D., Corrigan, C., Nguyen, H., Stone, E.A., Schauer, J.J., Carmichael, G., 2007. Atmospheric brown clouds: Hemispherical and regional variations in long-range transport, absorption, and radiative forcing. Journal of Geophysical Research: Atmospheres 112. doi: 10.1029/2006JD008124.

Sakai, T., Nagai, T., Nakazato, M., Mano, Y., Matsumura, T., 2003. Ice clouds and Asian dust studied with lidar measurements of particle extinction-to-backscatter ratio, particle depolarization, and water-vapor mixing ratio over Tsukuba. Applied Optics 42, 7103-7116. doi: 10.1364/AO.42.007103.

Sakai, T., Shibata, T., Iwasaka, Y., Nagai, T., Nakazato, M., Matsumura, T., Ichiki, A., Kim, Y.-S., Tamura, K., Troshkin, D., 2002. Case study of Raman lidar measurements of Asian dust events in 2000 and 2001 at Nagoya and Tsukuba, Japan. Atmospheric Environment 36, 5479-5489. doi: 10.1016/S1352-2310(02)00664-7.

Satheesh, S., Moorthy, K.K., 2005. Radiative effects of natural aerosols: A review. Atmospheric Environment 39, 2089-2110. doi: 10.1016/j.atmosenv.2004.12.029.

Seo, S., Kim, J., Lee, H., Jeong, U., Kim, W., Holben, B., Kim, S.-W., Song, C., Lim, J., 2015. Estimation of PM 10 concentrations over Seoul using multiple empirical models with AERONET and MODIS data collected during the DRAGON-Asia campaign. Atmospheric Chemistry and Physics 15, 319-334. doi: 10.5194/acp-15-319-2015.

Shin, D.H., Müller, D., Choi, T., Noh, Y.M., Yoon, Y.J., Lee, K.H., Shin, S.K., Chae, N., Kim, K., Kim, Y.J., 2014. Influence of wind speed on optical properties of aerosols in the marine boundary layer measured by ship-borne DePolarization Lidar in the coastal area of Korea. Atmospheric Environment 83, 282-290. doi: 10.1016/j.atmosenv.2013.10.027.

Shin, S.-K., Lee, K.-H., 2016. Modelling of Aerosol Vertical Distribution during a spring season at Gwangju, Korea. Asian Journal of Atmospheric Environment 10, 13-21. doi: 10.5572/ajae.2016.10.1.013.

Shin, S.-K., Müller, D., Lee C., Lee, K., Shin, D., Kim, Y., Noh, Y., 2015. Vertical variation of optical properties of mixed Asian dust/pollution plumes according to pathway of airmass transport over East Asia. Atmospheric Chemistry and Physics 15, 6707-6720. doi: doi:10.5194/acp-15-6707-2015.

Sugimoto, N., Lee, C.H., 2006. Characteristics of dust aerosols inferred from lidar depolarization measurements at two wavelengths. Applied Optics 45, 7468-7474. doi: 10.1364/AO.45.007468.

Tatarov, B., Müller, D., Noh, Y.M., Lee, K.H., Shin, D.H., Shin, S.K., Sugimoto, N., Seifert, P., Kim, Y.J., 2012. Record heavy mineral dust outbreaks over Korea in 2010: Two cases observed with multiwavelength aerosol/depolarization/Raman-quartz lidar. Geophysical Research Letters 39. doi: 10.1029/2012GL051972.

Wandinger, U., 2005. Introduction to lidar, in Lidar, Springer, New York, pp. 1-18. doi: 10.1007/0-387-25101-4_1.

Wong, M.S., Nichol, J.E., Lee, K.H., 2009. Modeling of aerosol vertical profiles using GIS and remote sensing. Sensors 9, 4380-4389. doi: 10.3390/s90604380.

Yu, X., Cheng, T., Chen, J., Liu, Y., 2006. A comparison of dust properties between China continent and Korea, Japan in East Asia. Atmospheric Environment 40, 5787-5797. doi: 10.1016/j.atmosenv.2006.05.013.

Zhai, P., Eskridge, R.E., 1997. Atmospheric water vapor over China. Journal of Climate 10, 2643-2652. doi: 10.1175/1520-0442(1997)010<2643:AWVOC>2.0.CO;2.

Table captions

Table 1 List of instrument, site information, aerosol parameter, and data availability used in this study.

Table 2 Average and standard deviation of Ångström exponent (440 nm/870 nm wavelength pair), PM_{10} concentration, and precipitable water contents for each classified episode at Gwangju, Korea during a spring season (March to May) of 2009, respectively.

Table 3 Average and standard deviation of aerosol characteristics for each classified episode obtained from AERONET over Gwagnju, Korea during a spring season (March to May) of 2009.

Table 4 Average and standard deviation of aerosol optical depth obtained from LIDAR, CIMEL sun/sky radiometer, and MODIS (Terra and Aqua) for each individual episode at Gwangju, Korea during a spring season (March to May) of 2009, respectively.

Table 5 Mean values and standard deviation of AOD derived from LIDAR and CIMEL Sun/sky radiometer, surface PM_{10} concentration, and Root mean square differences between the AOD retrieved with two instruments.

Figure captions

Fig. 1. Geographic location of observation site at Gwangju (35.23°N, 126.84°E).

Fig. 2. Schematic diagram of the dual polarization LIDAR used in this study.

Fig. 3. Temporal variation of (a) PM_{10} concentrations (olive triangle), (b) Ångström exponent (440 nm/870 nm wavelength pair, green pentagon), and (c) Precipitable water contents (purple diamond) during a spring season of 2009 at Gwangju, Korea. The red boxes indicate the high-PM_{10} episodes.

Fig. 4. MODIS-derived aerosol optical depth (AOD) combined MODIS RGB color composite image for each individual high-PM_{10} episode occurred on (a-c) 14~16 March 2009, (d-f) 5~6 April 2009, and (g-i) 4~6 May 2009, respectively.

Fig. 5. Air mass sources from 120-hours backward trajectories on (a) 16 March 2009, (b) 7 April 2009, and (c) 5 May 2009 for aerosol layers at altitude of 1.8 km, 2.0 km, and 2.2 km (purple, cyan, and yellow), respectively.

Fig. 6. Contour plot of range-corrected signal and depolarization ratio of aerosol observed by LIDAR during (a), (b) March 2009, (c), (d) April 2009, and (e), (f) May 2009 at Gwangju, Korea. Red colored box indicates that high-PM_{10} events occur.

Fig. 7. Mean vertical profiles of extinction coefficients measured by LIDAR at Gwangju, Korea for (red) the episode I, (green) episode II, (blue) episode III, and (magenta) other cases during total observation period. The mean values of scaling height for each individual case are also shown.

Fig. 8. AERONET retrieval of mean values of aerosol characteristics, (a) single scattering albedo (red square), (b) asymmetric factor (green circle), (c) real part of refractive index (blue triangle), and (d) imaginary part of refractive index (magenta diamond) as change with wavelength obtained Gwangju, Korea during a spring season (March to May) of 2009. The error bar indicates the standard deviations.

Fig. 9. Temporal variation of aerosol optical depth obtained by (a) LIDAR and (b) CIMEL sun/sky radiometer and MODIS (Terra and Aqua) during a spring season (March to May) of 2009 at Gwangju, Korea. The red box indicates that the high-PM_{10} concentration events occur.

Fig. 10. Scatterplot of AOD from LIDAR versus AOD from AERONET Sun/sky radiometer with respect to corresponding PM_{10} concentrations (a) higher than 100 $\mu g/m^3$ (b) less than 100 $\mu g/m^3$. The PM_{10} concentrations are denoted by different color and size of symbol.

Tables

[1]

Instrument	Region of Interest	Derived parameters	Available data
Dual polarization LIDAR	35.23°N, 126.84°E, 53 m	Extinction coefficient, Backscatter coefficient, AOD, Depolarization ratio	4, 6~21, 24~31/March/2009; 1~30/April/2009; 1~31/May/2009
Sun/sky radiometer	35.23°N, 126.84°E, 75 m	AOD, Ångström exponent, Precipitable water, Single Scattering Albedo, Asymmetric factor, Refractive index	7,9,15~17, 19, 21~25,30~31/March/2009; 2, 4~12, 16~18/April/2009; 5~11,14,18~19,23,28~31/May/2009
Beta gauge	35.17°N, 126.89°E, 67 m	PM_{10} concentration	1/Mar/2009~31/May/2009
MODIS (Level 1b)	20° – 50°N, 110°–140°E	AOD	1/Mar/2009~31/May/2009

[2]

Classification	$Å_{440-870}$	PM_{10} [µg/m^3]	PWC [cm]

Episode I	0.77 ± 0.19	139 ± 70	0.53 ± 0.32
Episode II	1.36 ± 0.10	115 ± 21	0.77 ± 0.05
Episode III	1.33 ± 0.06	89 ± 7	0.81
Others	1.17 ± 0.26	46 ± 16	1.04 ± 0.45

[3]

Parameters (λ=440/675/870/1020 nm)	**Episode I**	**Episode II**
Ω	0.92 ± 0.01/0.95 ± 0.01/0.96 ± 0.01/0.96 ± 0.01	0.93 ± 0.01/0.92 ± 0.01/0.91 ± 0.01/0.89 ± 0.02
g	0.73 ± 0.02/0.69 ± 0.01/0.69 ± 0.02/0.70 ± 0.03	0.72 ± 0.01/0.65 ± 0.01/0.61 ± 0.02/0.60 ± 0.02
n	1.44 ± 0.02/1.47 ± 0.03/1.48 ± 0.02/1.47 ± 0.01	1.46 ± 0.03/1.48 ± 0.03/1.48 ± 0.03/1.48 ± 0.03
k	0.0046 ± 0.0002/0.0026 ± 0.0003/0.0025 ± 0.0003/0.0027 ± 0.0001	0.0090 ± 0.0013/0.0088 ± 0.0013/0.0093 ± 0.0018/0.0099 ± 0.0019
	Episode III	**Others**
Ω	0.92 ± 0.01/0.92 ± 0.01/0.92 ± 0.01/0.92 ± 0.01	0.93 ± 0.02/0.93 ± 0.02/0.92 ± 0.02/0.91 ± 0.03
g	0.70 ± 0.02/0.63 ± 0.03/0.61 ± 0.02/0.62 ± 0.02	0.71 ± 0.02/0.65 ± 0.03/0.63 ± 0.04/0.63 ± 0.04
n	1.40 ± 0.09/1.43 ± 0.05/1.45 ± 0.03/1.45 ± 0.02	1.45 ± 0.04/1.46 ± 0.03/1.47 ± 0.03/1.47 ± 0.03
k	0.0085 ± 0.0013/0.0069 ± 0.0019/0.0061 ± 0.0021/0.0061 ± 0.0021	0.0076 ± 0.0025/0.0069 ± 0.0024/0.0070 ± 0.0026/0.0075 ± 0.0029

[4]

Classification	τ_{LIDAR}	τ_{CIMEL}	τ_{MODIS}
			TERRA/AQUA
Episode I	0.52 ± 0.20	0.71 ± 0.42	0.77 ± 0.11/0.40 ± 0.14*
Episode II	0.44 ± 0.14	0.68 ± 0.26	0.66 ± 0.14/0.70 ± 0.16
Episode III	0.41 ± 0.07	0.44 ± 0.16	0.58 ± 0.07/0.56 ± 0.07
Others	0.38 ± 0.13	0.52 ± 0.34	0.51 ± 0.07/0.56 ± 0.07

[5]

Classification	**τ_{LIDAR}**	**τ_{CIMEL}**	**RMSD**	**PM_{10} concentration**
Case I (>100 μg/m^3)	0.48 ± 0.15	0.76 ± 0.18	28 ± 12%	137 ± 32 μg/m^3
Case II (<100 μg/m^3)	0.39 ± 0.13	0.43 ± 0.24	10 ± 10%	65 ± 21 μg/m^3

Figures

[1]

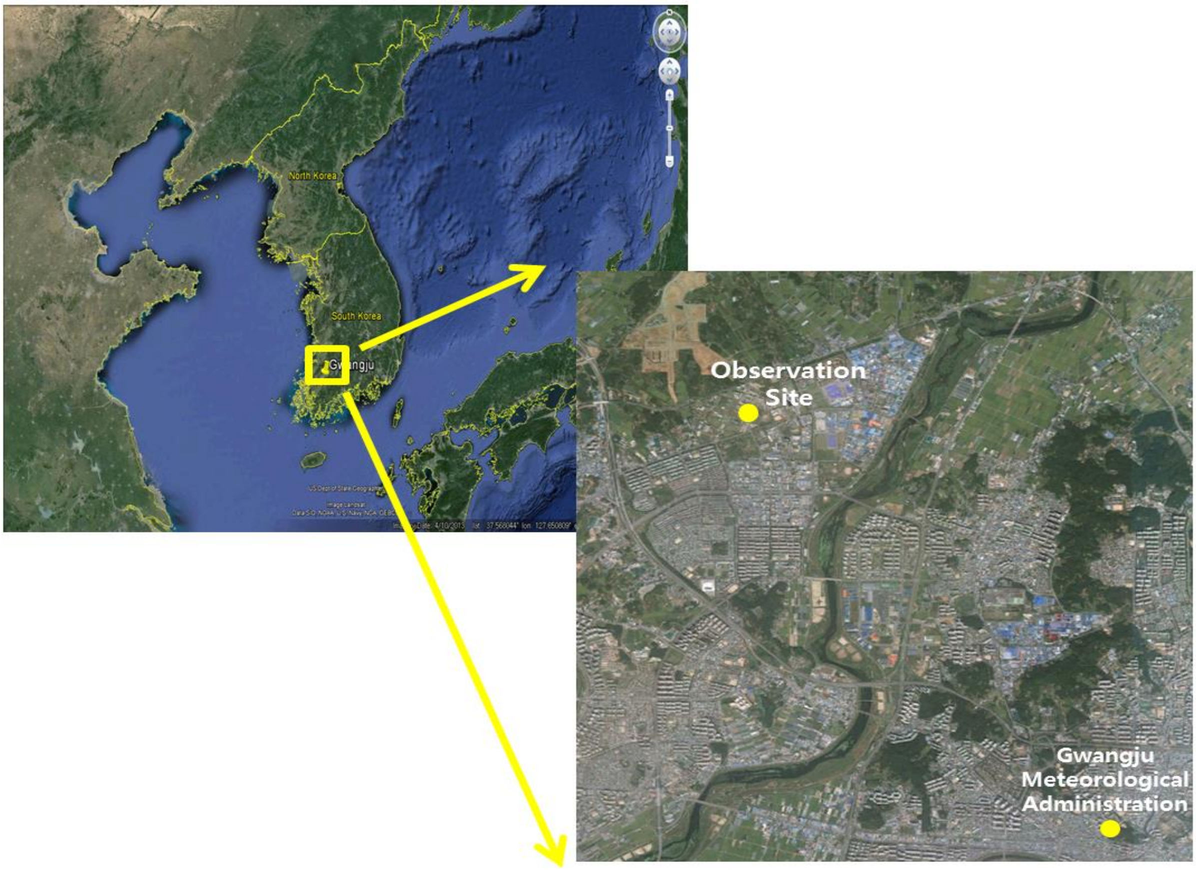
North Korea
South Korea
Gwangju
Observation Site
Gwangju Meteorological Administration

[2]

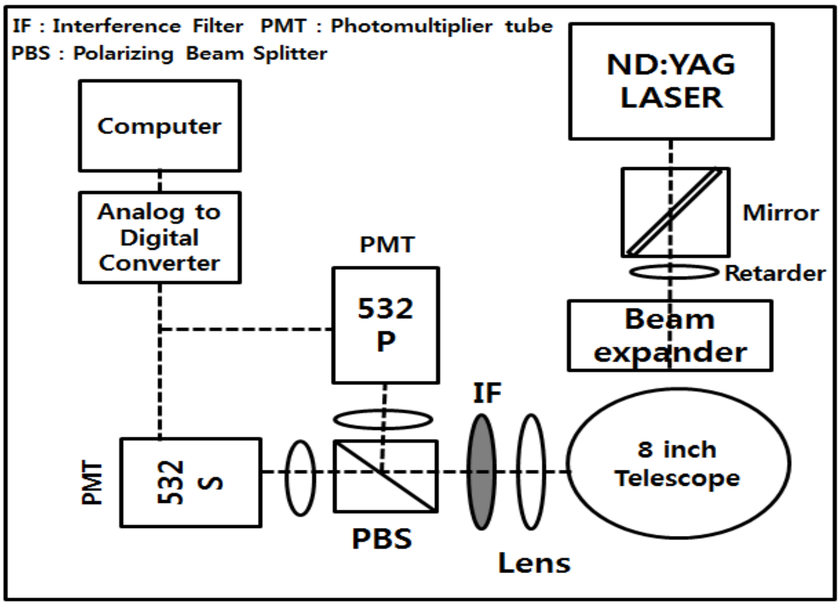
IF : Interference Filter PMT : Photomultiplier tube
PBS : Polarizing Beam Splitter
Computer
Analog to Digital Converter
ND:YAG LASER
Mirror
Retarder
Beam expander
PMT
532 P
IF
PMT
532 S
PBS
Lens
8 inch Telescope

[3]

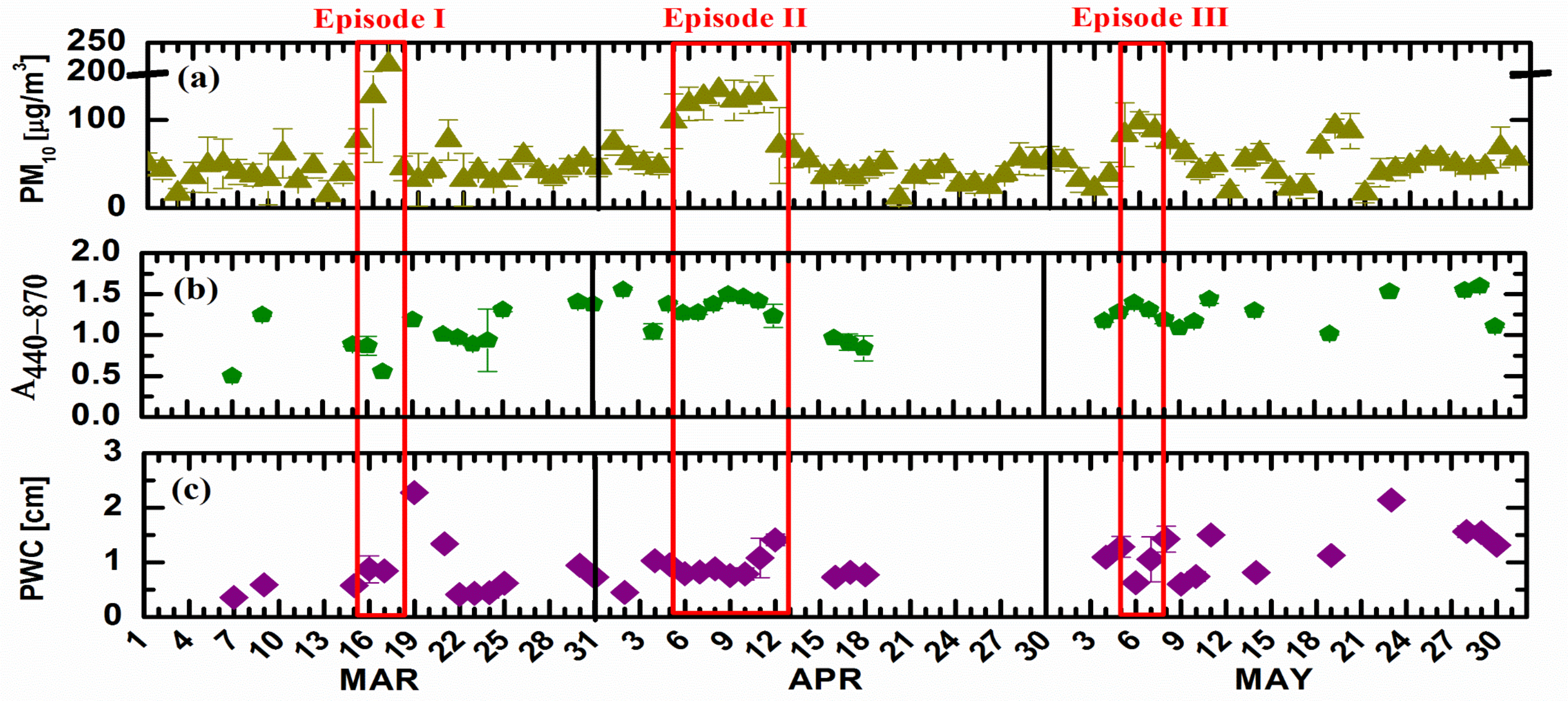
Episode I
Episode II
Episode III
(a)
PM$_{10}$ [μg/m^3]
250
200
100
0
(b)
A$_{440-870}$
2.0
1.5
1.0
0.5
0.0
(c)
PWC [cm]
3
2
1
0
1
4
7
10
13
16
19
22
25
28
31
3
6
9
12
15
18
21
24
27
30
3
6
9
12
15
18
21
24
27
30
MAR
APR
MAY

[4]

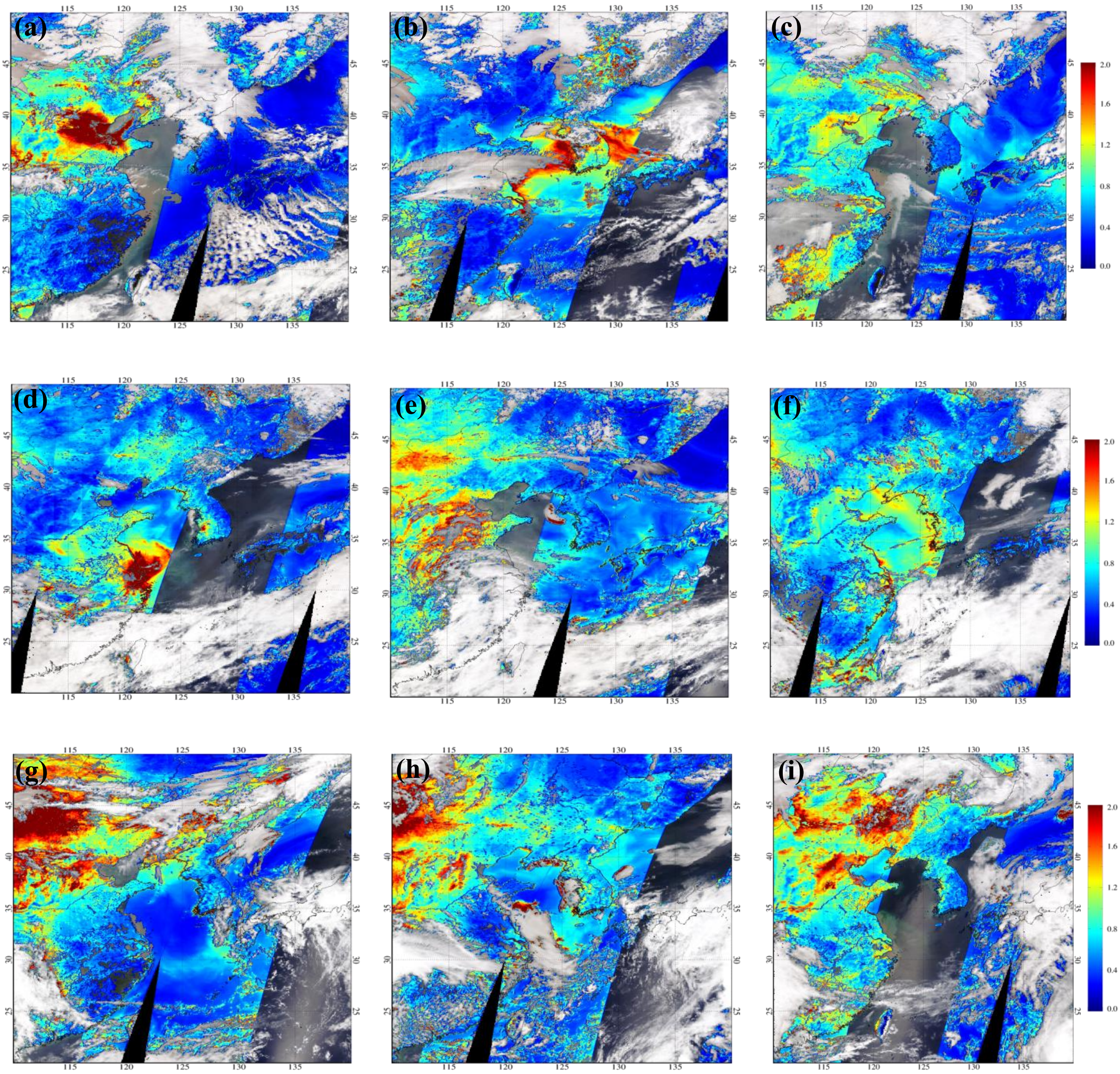

[5]

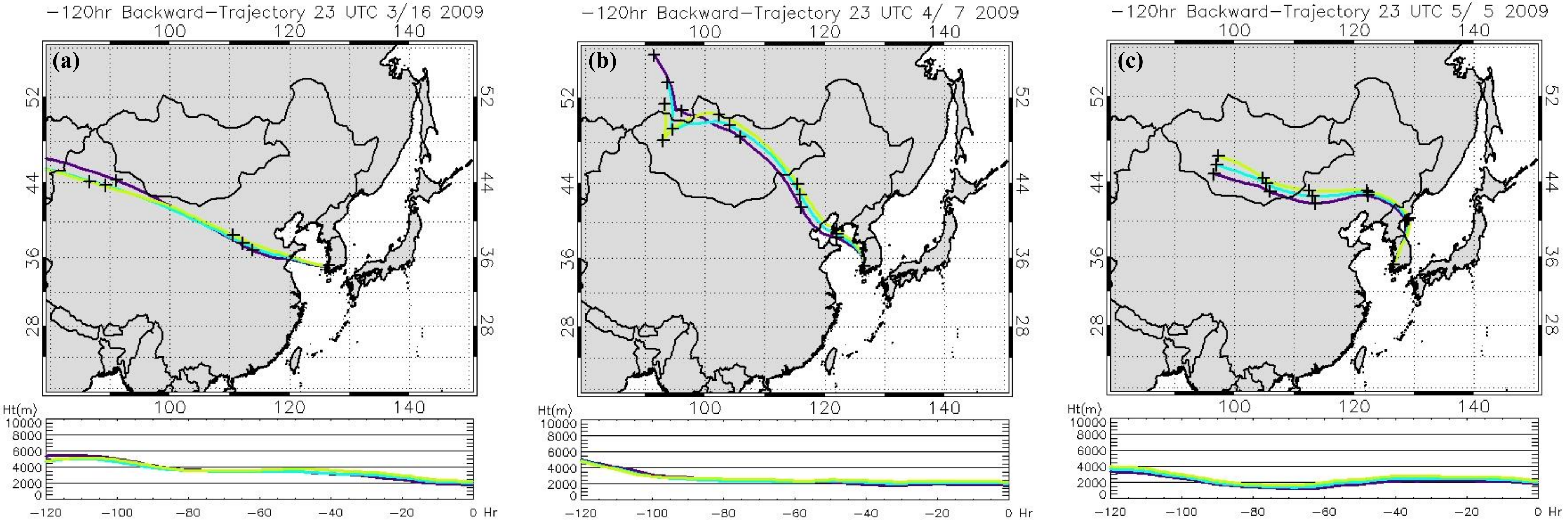
−120hr Backward−Trajectory 23 UTC 3/16 2009
(a)
−120hr Backward−Trajectory 23 UTC 4/ 7 2009
(b)
−120hr Backward−Trajectory 23 UTC 5/ 5 2009
(c)
100
120
140
52
44
36
28
Ht(m)
10000
8000
6000
4000
2000
0
−120
−100
−80
−60
−40
−20
0 Hr

[6]

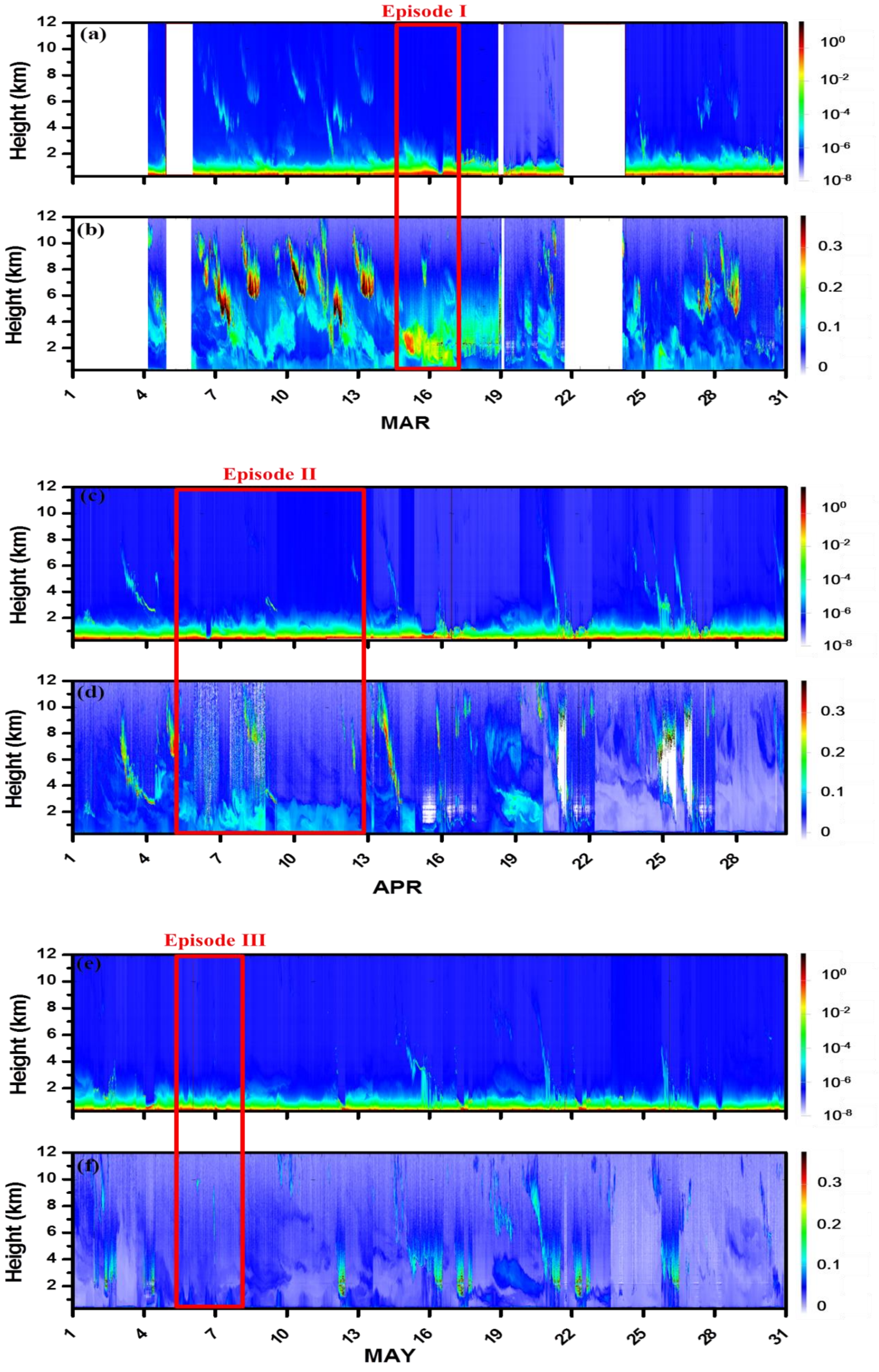
Episode I
(a)
(b)
Height (km)
12
10
8
6
4
2
10^0
10^{-2}
10^{-4}
10^{-6}
10^{-8}
0.3
0.2
0.1
0
1
4
7
10
13
16
19
22
25
28
31
MAR
Episode II
(c)
(d)
APR
Episode III
(e)
(f)
MAY

[7]

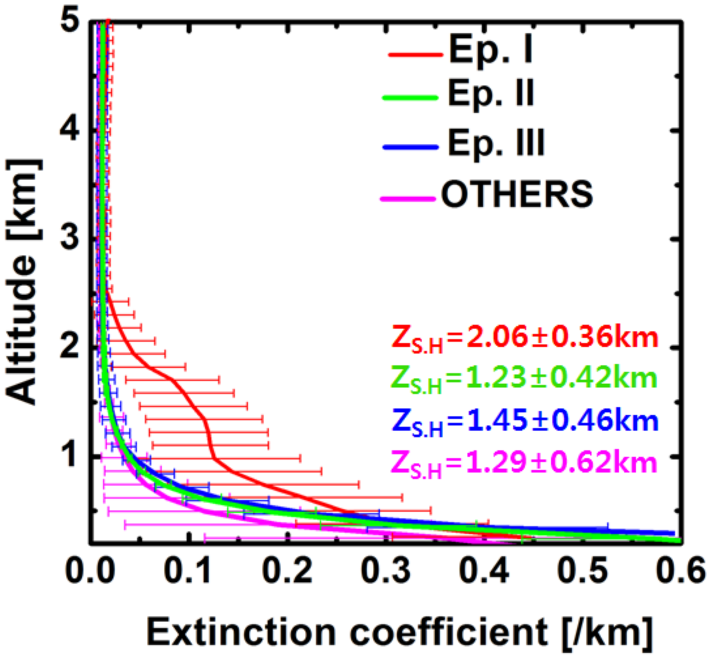
Ep. I
Ep. II
Ep. III
OTHERS
$Z_{S.H}$=2.06±0.36km
$Z_{S.H}$=1.23±0.42km
$Z_{S.H}$=1.45±0.46km
$Z_{S.H}$=1.29±0.62km
Altitude [km]
Extinction coefficient [/km]
0.0
0.1
0.2
0.3
0.4
0.5
0.6
1
2
3
4
5

[8]

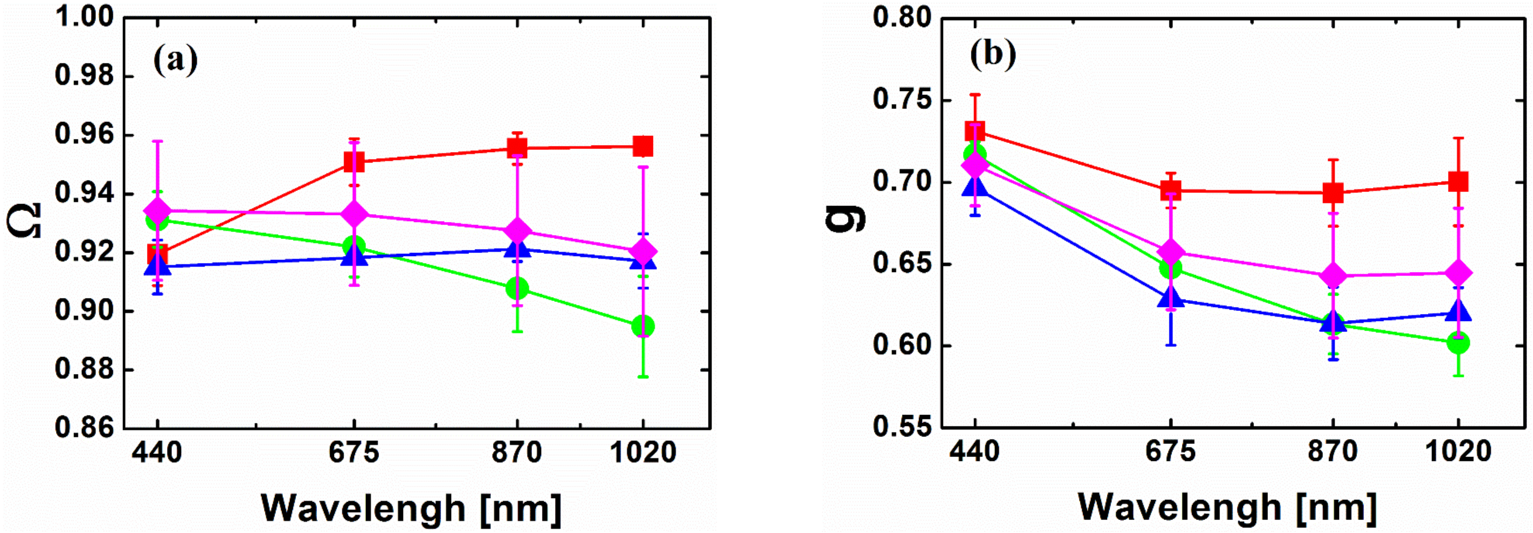
(a)
Ω
1.00
0.98
0.96
0.94
0.92
0.90
0.88
0.86
440
675
870
1020
Wavelengh [nm]
(b)
g
0.80
0.75
0.70
0.65
0.60
0.55
440
675
870
1020
Wavelengh [nm]

[9]

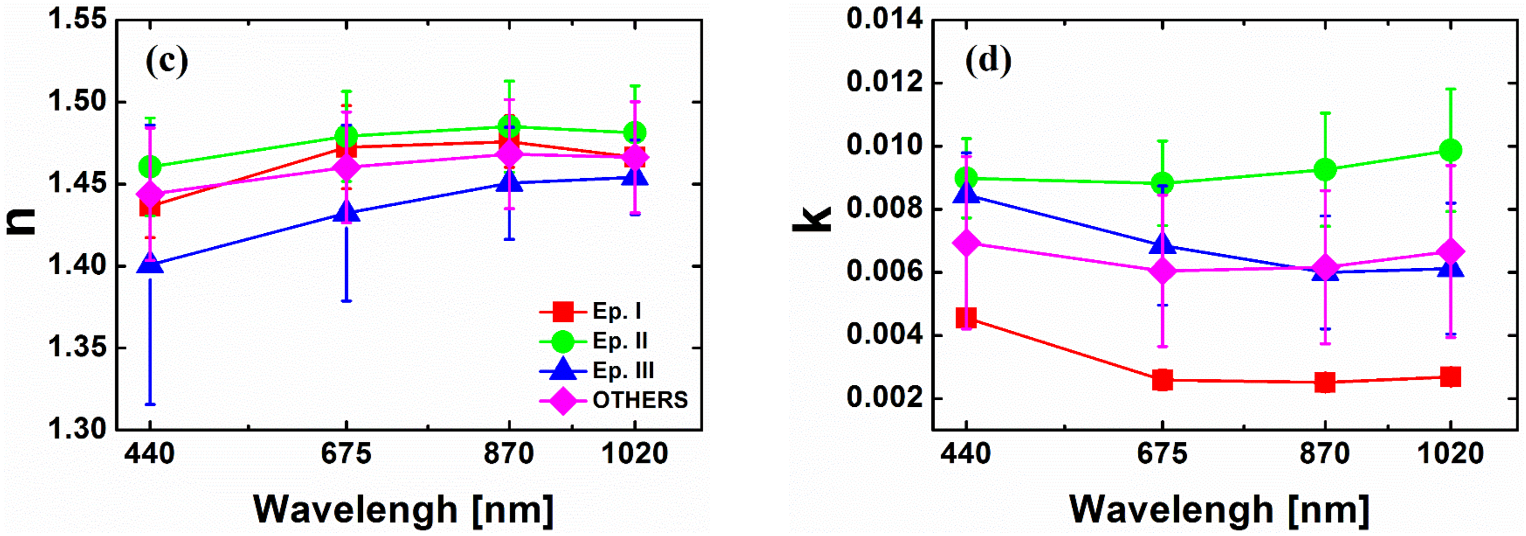
(c)
n
1.55
1.50
1.45
1.40
1.35
1.30
440
675
870
1020
Wavelengh [nm]
Ep. I
Ep. II
Ep. III
OTHERS
(d)
k
0.014
0.012
0.010
0.008
0.006
0.004
0.002
440
675
870
1020
Wavelengh [nm]

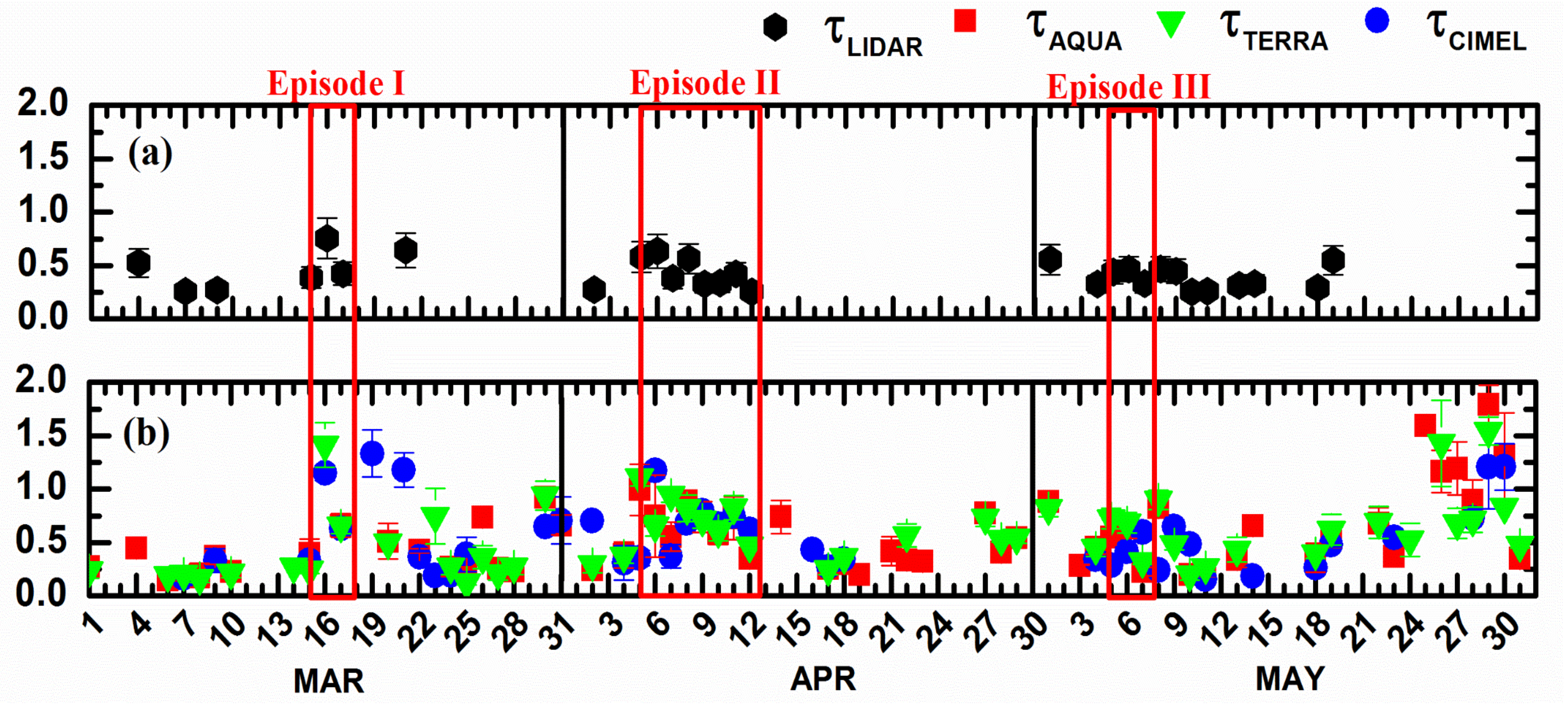

τ_{LIDAR}
τ_{AQUA}
τ_{TERRA}
τ_{CIMEL}
Episode I
Episode II
Episode III
(a)
(b)
2.0
1.5
1.0
0.5
0.0
1
4
7
10
13
16
19
22
25
28
31
3
6
9
12
15
18
21
24
27
30
MAR
APR
MAY

[10]

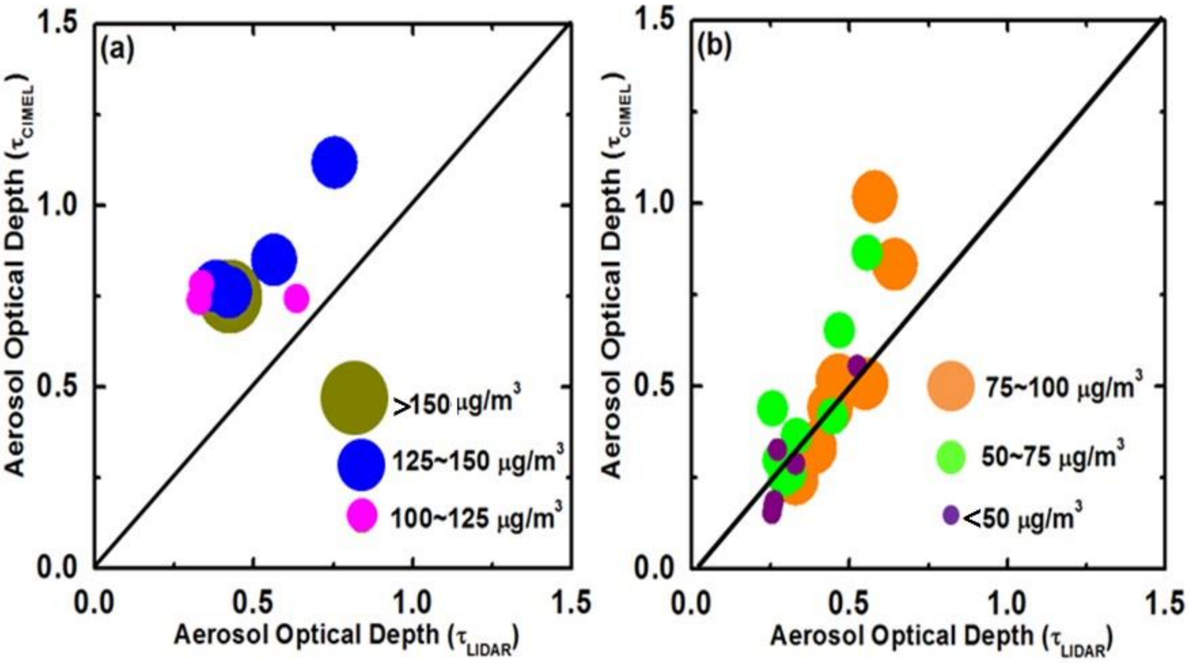
(a)
Aerosol Optical Depth (τ_{CIMEL})
Aerosol Optical Depth (τ_{LIDAR})
0.0
0.5
1.0
1.5
>150 μg/m³
125~150 μg/m³
100~125 μg/m³
(b)
Aerosol Optical Depth (τ_{CIMEL})
Aerosol Optical Depth (τ_{LIDAR})
0.0
0.5
1.0
1.5
75~100 μg/m³
50~75 μg/m³
<50 μg/m³